communications earth & environment

Article

A Nature Portfolio journal

https://doi.org/10.1038/s43247-026-03486-z

# Sea-ice ridge formation fuels Arctic pelagic food webs during the polar night



Lasse Mork Olsen[1,2] ✉, Evgenii Salganik[3,4], Oliver Müller[1], Luisa von Albedyll[4], Philipp Assmy[3], Mats A. Granskog[3,5], Clara J. M. Hoppe[4], Robert G. Campbell[6], Aud Larsen[7], Eva Leu[8], Rolf Gradinger[9], Jessie Gardner[9], Nicole Aberle[10,11], Dmitry V. Divine[3], Knut V. Høyland[12], Christian Katlein[4], Benjamin A. Lange[3,13], Agnieszka Tatarek[14], Jozef Wiktor[14] & Gunnar Bratbak[1]

There is no light for photosynthesis by phytoplankton and sea-ice algae during the polar night, but microbial grazers remain active through the dark winter months in the Arctic Ocean. Where the energy to sustain these organisms comes from is unknown. Here we observed active tintinnid ciliates during the polar night, heterotrophic protists known to feed on phytoplankton and smaller heterotrophic protists. Our calculations indicate that the pelagic microbial loop transferring energy from bacterial production through microbial grazers was not sufficient to sustain the observed tintinnid biomass. However, the sea ice contained frozen-in particulate organic carbon produced during the previous growth seasons. We show that enough food particles can be released by mechanical break-up during sea-ice ridging, which together with bacterial production, sustained the observed tintinnid biomass in the water column. This is an important but overlooked mechanism for winter survival of plankton in the Arctic Ocean.

The basic structure and functioning of the microbial food web of Arctic Ocean surface waters is the same as in other oceans. The main primary producers are photosynthetic phytoplankton, but with a substantial, regionally highly variable contribution from ice algae[1]. Depending on their size, algae are primarily consumed by metazoan (e.g., copepods) or protist grazers (ciliates and dinoflagellates). Algae and their grazers release dissolved organic matter, which is an energy source for pelagic heterotrophic bacteria, which subsequently are food for heterotrophic pico- and nanoflagellates which again can be food for heterotrophic ciliates and dinoflagellates, forming a microbial loop[2,3].

The temperature in the surface waters of the ice-covered Arctic Ocean is around the freezing point of seawater (−1.8 ± 1 °C) all year round[4]. Microorganisms adapted to the Arctic Ocean can grow at these temperatures[5–7]. However, at latitudes above 84°N the sun is 18° below the horizon at winter solstice and the dark period lasts up to 177 days. During this long period without direct sunlight, often called the polar night, virtually no phototrophic primary production is possible due to insufficient irradiance for photosynthesis[8,9]. Thus, one major challenge for pelagic consumers during the polar night is the lack of photosynthetic primary production, i.e., the lack of freshly produced organic energy input to the food web.

During the SHEBA expedition in the western part of the central Arctic Ocean, Sherr et al.[10] observed that the abundances of bacteria and heterotrophic protists doubled in concert with an increase in phytoplankton biomass from winter to summer. Gosselin et al.[1] confirmed that heterotrophic dinoflagellates dominated protist biomass in the central Arctic Ocean in the summer, in abundance ranges same as Sherr et al.[10] measured. The low, but still persistent stocks of microbes recorded during winter, were dominated by prokaryotes and heterotrophic protists, mainly dinoflagellates, reaching biomasses about half of summer concentrations[10]. Vaque et al.[11] also observed a dominance of prokaryotes and heterotrophic protists in the winter plankton with biomasses about half of the summer values while the winter stocks of phototrophs amounted to only 20% of the summer biomass during their seasonal CASES study in Franklin Bay in the western Arctic. Ciliates had generally low abundance but persisted through the winter with a biomass close to summer levels. Bacterial abundance and production were maintained at 30% and 10% of summer levels, respectively, throughout the winter. While

[1]University of Bergen, Dept. of Biosciences, Bergen, Norway. [2]Aqua Kompetanse, Flatanger, Norway. [3]Norwegian Polar Institute, Fram Centre, Tromsø, Norway. [4]Alfred Wegener Institute, Helmholtz Centre for Polar and Marine Research, Bremerhaven, Germany. [5]Hanse-Wissenschaftskolleg Institute of Advanced Study, Delmenhorst, Germany. [6]University of Rhode Island, Narragansett, USA. [7]NORCE Norwegian Research Centre AS, NORCE Environment, Bergen, Norway. [8]Akvaplan-niva, Fram Centre, Tromsø, Norway. [9]UiT The Arctic University of Norway, Department of Arctic and Marine Biology, Tromsø, Norway. [10]Norwegian University of Science and Technology, Dept. of Biology, Trondheim, Norway. [11]Institute of Marine Ecosystem and Fishery Science (IMF), Hamburg University, Hamburg, Germany. [12]Norwegian University of Science and Technology, Department of Civil and Environmental Engineering, Trondheim, Norway. [13]Norwegian Geotechnical Institute, Oslo, Norway. [14]Institute of Oceanology, Polish Academy of Sciences, Sopot, Poland. ✉e-mail: lasse@aqua-kompetanse.no

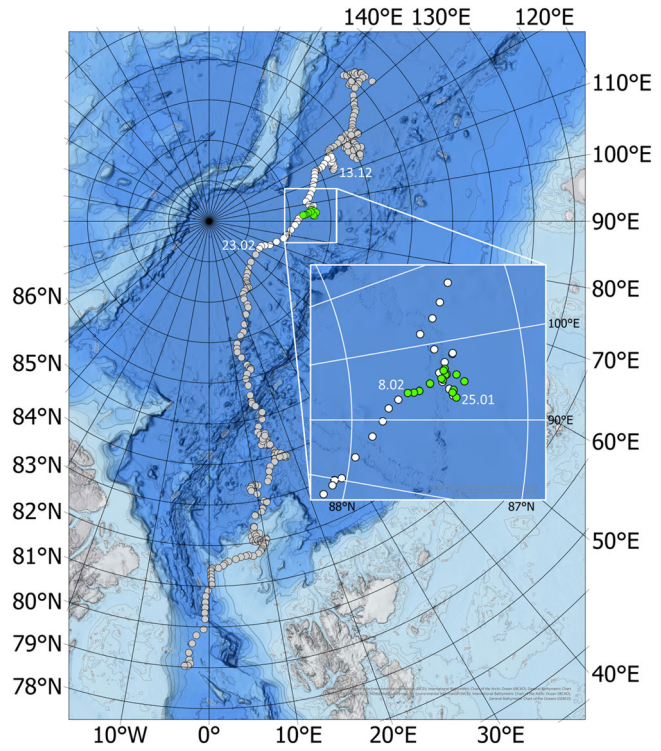


**Fig. 1 | Map of the Arctic Ocean showing the MOSAiC drift track.** The drift track is indicated with one circle for each day. The white circles indicate the period with field sampling for this study (December 13, 2019, to February 23, 2020), and green circles the period when we observed active tintinnids in the water column under the ice using a plankton net attached to a remotely operated vehicle (ROV) (January 25 to February 8, 2020). The basemap used is Arctic Bathymetric Contours (IBCAOv4/GEBCO_2020)[98].

the higher bacterial production in summer was correlated with photosynthetic activity, the observed abundance and activity levels in winter can to some extent be supported by refractory dissolved organic matter remaining after the productive season[12] sufficient to sustain bacterivory by heterotrophic flagellates < 5 µm[11]. Ciliates cannot starve for more than a few days before dying or forming resting spores, while heterotrophic dinoflagellates can live without feeding for periods of several weeks[13]. Therefore, the persistence of active ciliate populations through the polar night suggests there must be food sources other than the winter microbial loop characterized by bacterivorous flagellates consuming a low bacterial production.

Sea ice can contain substantial amounts of organic matter[14,15] and is a porous medium because salts in seawater are concentrated into brine channels and pockets during freezing[16]. How open and connected these channels are, is determined by ice temperature and sea-ice bulk salinity[17]. First-, second- and multi-year sea ice that does not completely melt during summer becomes relatively warm, thin, and very porous. This "rotten" ice can thus get loaded with algae and various heterotrophic organisms from the water column and from growth within the ice. When this ice grows due to low temperatures in the autumn and winter the organic matter is locked up in a colder and thus impermeable layer in the upper part of the ice where porosity is low[15], seemingly inaccessible to the protists in the water column. However, the pack ice is constantly breaking up into ice floes or rubble fields due to surface ocean currents and wind stress[18]. Ice floes frequently collide and form pressure ridges[19]. Modeling suggests that sea-ice ridges constitute around 30% of the total Arctic sea-ice volume[20] and 25 to 45% of the area[21]. According to long-term ice thickness records in Fram Strait, a major export area of sea ice from the central Arctic Ocean, the fraction of ice that has experienced mechanical deformation amounted to 37 ± 8%[22].

During ridge formation, level sea-ice floes are broken up into ice blocks which, when submerged, form the keel of a ridge[19] and are subsequently warmed up to the ambient seawater temperature of about −1.8 °C. With a typical (practical) salinity of first-year ice ridges around 3–5[23], such temperature is well above the sea-ice percolation threshold of −5 °C at a bulk salinity of 5, enabling connection of brine channels through the ice making it permeable[17]. This means that organic particles inside the level ice that were previously trapped can be released into the water surrounding the ridge keel.

The Multidisciplinary drifting Observatory for the Study of the Arctic Climate (MOSAiC) expedition[24,25] (Fig. 1), provided a unique opportunity to study seawater and ice-associated biological processes, including sea-ice ridges[26], over a seasonal cycle in the Arctic Ocean (Fig. 2). Our observations during the polar night confirmed that heterotrophic dinoflagellates dominate the microbial food web biomass in the water column underneath the sea ice. More surprisingly, we also observed an active epipelagic population of the tintinnid ciliate *Ptychocylis obtusa*, which is a common species in the Arctic Ocean[27]. Dinoflagellates were presumably prey for the tintinnids; however, it was surprising that another trophic level was seemingly maintained by bacterial production (Fig. 3), which we measured to be very low. Based on our field data and basic modeling efforts, we elaborate on this winter heterotrophic activity by focusing on two research questions:

1) Could pelagic bacterial production sustain the stocks of heterotrophic protists that persisted during the polar night?

2) Is ice-associated organic matter, released by sea-ice deformation (ridging), an important additional food source for heterotrophic protists in the Arctic Ocean during the polar night?

## Results And Discussion

### Did bacterial production sustain protist grazers in the polar night?

From late January to early February at around 87°N there was no sunlight and close to zero primary production in the water column below sea ice[28], reflected by very low chlorophyll a (Chl a) concentrations (Table 1) in the same range as previously found in the polar night [8]. The winter protist community, dominated by the dinoflagellate (D), mostly Gymnodiniales (Supplementary Fig. 1), also confirmed abundances (Table 2) reported from other polar night expeditions[10,11]. In addition, we observed a monospecific population of tintinnid (T) ciliates, consisting of active *Ptychocylis obtusa* (Fig. 3 and Supplementary Fig. 2). Their abundance in the water below the ice was 14.7 ± 2.7 cells $L^{-1}$ (avg. ± SE) (Table 2) similar to the total tintinnid abundances, including *Ptychocylis* sp., in the Chukchi Sea[29,30], and *Ptychocylis obtusa* in the Barents Sea, during summer in periods with considerably higher primary production[31]. Whereas some heterotrophic dinoflagellates, like *Gymnodinium* sp., which can endure starvation for several weeks, ciliates only survive a few days without food[13]. The relatively high polar night abundance of tintinnids was therefore very surprising.

Although tintinnid abundances were similar to summer data reported elsewhere, this did not apply to other members of the microbial loop. The measured abundances of bacteria (B) and heterotrophic bacterivorous nanoflagellates (F; Table 2) were only about one tenth of what has been observed in summer in the Arctic Ocean[11,12]. Bacterial carbon production was on average as low as 49 ± 1.5 ng C $L^{-1}$ $d^{-1}$ (Table 2) and in agreement with previous polar night observations[8]. Arctic pelagic bacterial production rates are often related to primary production and/or algal biomass and are therefore expected to be low in the winter season and especially during polar night, when small heterotrophic bacteria like SAR11 and chemoautotrophic archaea and bacteria dominate[12,32], while higher rates in the order of 1 µg C $L^{-1}$ $d^{-1}$ are observed in summer[33]. Berge et al. (Berge et al. 2015) concluded that microbial activity and maintenance of the microbial community through the polar night, although in low concentrations, are likely sustained by organic matter produced during the previous summer.

To assess whether the low bacterial production we measured could be sufficient to sustain the observed heterotrophic protist food web culminating in tintinnid ciliates, we used steady state mass balance calculations (Eqs. 1–5). The low and stable values for chlorophyll concentration (phytoplankton biomass) and abundances of organisms at each trophic level during the study period (Tables 1 and 2), the low bacterial growth rate

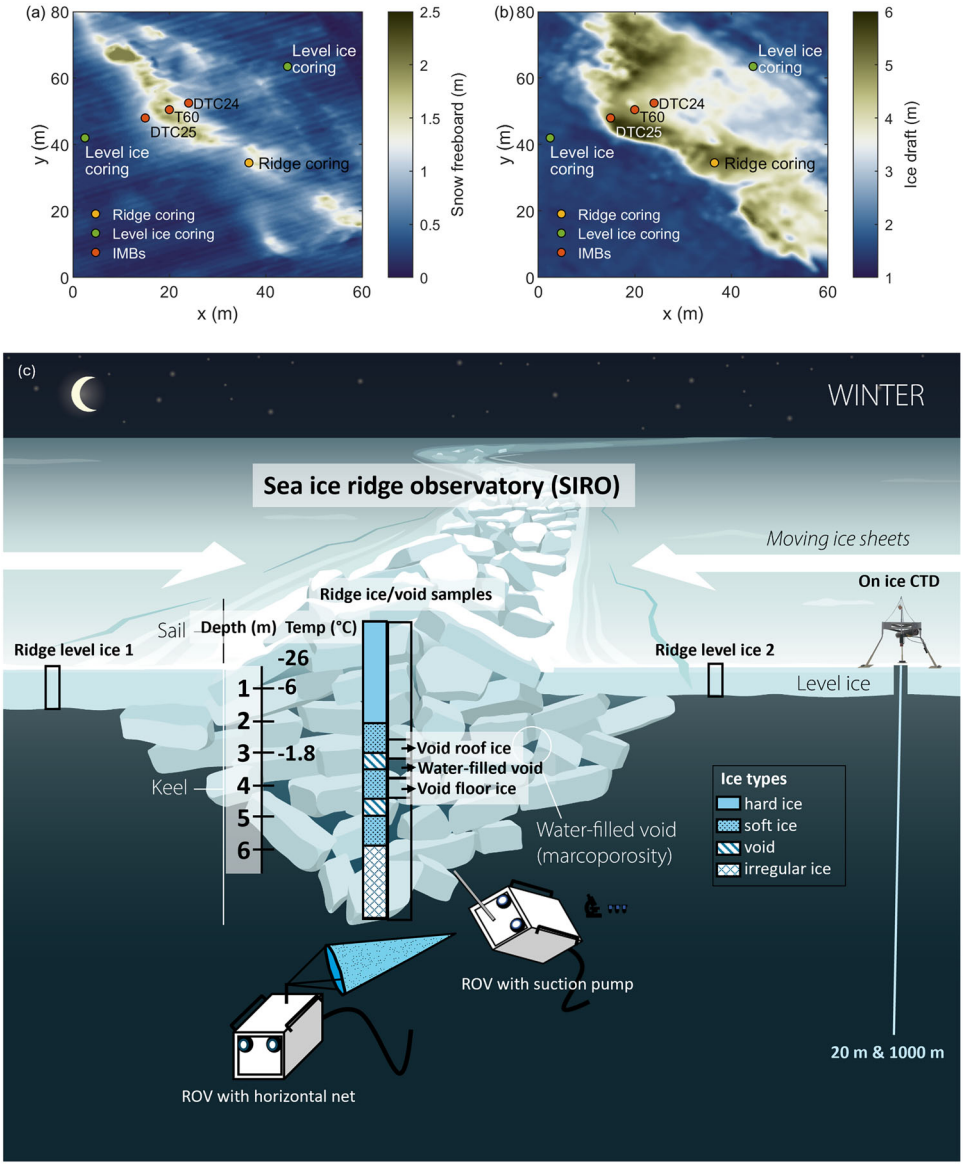


**Fig. 2 | Locations of coring sites and ice mass balance buoys at the sea-ice ridge studied. a** Coring sites and ice mass balance buoys (IMB) at the studied ridge (Fort Ridge) shown on a contour plot of snow or ice freeboard (height over water level) on 7 January, measured by an airborne laser scanner [94]. **b** The ice draft on 7 January was measured by a multibeam sonar[99]. **c** Schematic overview of the sea-ice ridge observatory (SIRO) set up at Fort Ridge, with the sampling sites, the sampling methods and the various samples taken. A simplified characterization of ridge structure and sample types through a core taken in the ridge keel as described in Methods is also shown. See Fong et al.[25] for a map of sampling sites in the MOSAiC Central Observatory ice floe.

(Table 2), and the stable environmental conditions, e.g., temperature and irradiance during the polar night, suggest that the microbial ecosystem in the water column was close to steady state. In a steady state the growth rate of prey organisms is determined by predation, i.e., the clearance rate (CR) of the predator, derived from carbon demandas shown in Eqs. 1–5. We estimated the carbon demand for each trophic levels/ functional groups of the microbial food web as observed in this study. In general, carbon biomass production (P; g C $L^{-1}$ $d^{-1}$) is given by:

$$P = \mu N \quad (1)$$

where μ is specific growth rate ($d^{-1}$) and N is carbon biomass (g C $L^{-1}$). Then the carbon demand (I; g C $L^{-1}$ $d^{-1}$) for all organisms is given by:

$$I = \frac{P}{Y} \quad (2)$$

where Y is the growth yield, i.e., the fraction of carbon intake turned into predator biomass. The carbon demand (I) can also be expressed as:

$$I = (CR_{predator} N_{predator}) N_{prey} \quad (3)$$

where CR is carbon biomass specific clearance rate (L $gC^{-1}$ $d^{-1}$) and N is carbon biomass. Then

$$CR = \frac{I_{predator}}{N_{predator} N_{prey} S} \quad (4)$$

where S is the selectivity coefficient for the prey (tintinnid selectivity for bacteria: TSB and for flagellates: TSF, and dinoflagellates selectivity for bacteria: DSB), as a fraction of full selectivity. The growth rates of the prey, i.e., flagellates and bacteria, is given by the biomass specific clearance rate and biomass of their predators, tintinnids and flagellates, respectively:

$$\mu_{prey} = CR_{predator} N_{predator} \quad (5)$$

Because the growth rate of the tintinnids was unknown we inserted a range of growth rates to calculate the carbon demand (Fig. 4a), and the clearance rate needed to obtain that amount of carbon from prey organisms (Fig. 4b), which again determined the growth rate of the prey (Fig. 4c)

We assumed that the tintinnids (T) were feeding on dinoflagellates (D) which had an optimal prey size, with a selectivity coefficient of one, and assumed their selectivity coefficient for nanoflagellates (F) being 0.5 (TSF, tintinnid selectivity for flagellates) due to their smaller and less optimal size.

The tintinnid selectivity for bacteria (B) was set to 0.01 (TSB, tintinnid selectivity for bacteria) because of their even smaller and less optimal size[34]. We further assumed that D fed on F with a selectivity of one and on B with a selectivity of 0.2 (DSB, dinoflagellates selectivity for bacteria)[34], and F fed only on B (Fig. 4d). We set the growth yield (Y) i.e., fraction of carbon intake turned into predator carbon, for tintinnids, flagellates and dinoflagellates to 0.4[35–37], and to 0.5 for bacteria[38].

The maximum clearance rate (CR) previously measured for tintinnids is approximately 0.5 mL cell$^{-1}$ day$^{-1}$[39]. We set $CR_T$ to this 0.5, and in Fig. 4 added guidelines showing that the steady state equations then give a tintinnid growth rate of 0.09 d$^{-1}$ (Fig. 4b). This is equivalent to a doubling time of 7.7 days. The $CR_D$ is then 0.382 µL cell$^{-1}$ day$^{-1}$ (Fig. 4b), which is within the CR measured for 20 µm diameter *Gymnodinium* sp. by Jakobsen and Hansen (1997). However, the $CR_F$ needed to sustain the carbon demand of D would be 0.128 µL cell$^{-1}$ day$^{-1}$, which is considerably higher than the range previously measured for bacterivorous nanoflagellates of 0.025 to 0.050 µL cell$^{-1}$ day$^{-1}$[35,40]. Under steady state conditions, this predation rate infers a bacterial growth rate of 0.013 d$^{-1}$ (Fig. 4c), same as the growth rate calculated from measured bacterial production (BP/biomass) of 0.013 ± 0.0004 d$^{-1}$. This implies a bottleneck in the flow of carbon from B to higher trophic levels at the level of F (Fig. 4d), where F can, at the maximum, deliver about one-third of the carbon demand according to the known maximum $CR_F$.

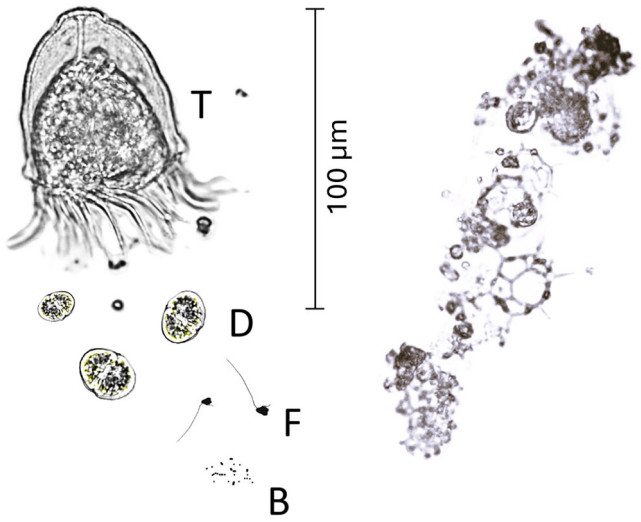


**Fig. 3 | The active organisms dominating the epipelagic microbial food web during the polar night.** The groups of active organisms at different trophic levels include heterotrophic bacteria (B), heterotrophic nanoflagellates (F), heterotrophic dinoflagellates (D) and tintinnids (T) of the species *Ptychocylis obtusa*. At the right side is shown an aggregate of various cells and organic matter frozen into sea ice.

Our growth yield parameter (Y) is equivalent to gross growth efficiency (GGE). $Y_B$ only affects the bacterial carbon demand and not the carbon flow to higher trophic levels in the steady state model, so it is not discussed further. The yield value of 0.4 set for all the predators is an approximation based on the literature for protists including tintinnids, dinoflagellates and bacterivorous flagellates[35–37]. To account for the possible variation of Y we performed a sensitivity analysis with a parameter sweep where Y varied between 0.2 and 0.8 for F, D and T, respectively, one at a time while it was constant at 0.4 for the other two and the predation selectivity coefficients were held constant at the values shown in Fig. 4. $CR_T$ was held constant at 0.5 mL cell$^{-1}$ day$^{-1}$. Increasing $Y_T$ gives an increased growth rate for T but does not affect growth rates or CR for the other trophic levels (Supplementary Fig. 3). Increasing $Y_D$ results in reduced growth rates for F and B because the carbon demand for D is reduced, and it gives a reduction in $CR_F$ because the carbon flow through F is reduced. At an unrealistically high $Y_D = 0.8$, $CR_F$ equals 104 nL cell$^{-1}$ d$^{-1}$ (Supplementary Fig. 3), i.e., it is reduced but still double the maximum values measured previously[35,40].

A parameter sweep for the prey selectivity coefficients shows that the effect of increasing the selectivity of T for F and B (TSF and TSB) gives an increased growth rate of T when $CR_T$ is constant but have only small effects on growth rate or CR of F and D (Supplementary Fig. 4). Increasing D's selectivity for B (DSB) had a more marked effect on the CR of both D and F, which was reduced because D obtained more carbon from B. $CR_F$ was reduced to 87 nL cell$^{-1}$ d$^{-1}$ when DSB = 1, i.e., maximal selectivity (Supplementary Fig. 4). D consisted mostly of *Gymnodinium* sp.

**Table 1 | Range of chlorophyll a (Chl a) concentrations in sea-ice and water**

| Sample site | Chl a (mg m$^{-3}$) | Description |
|---|---|---|
| Water 20 m | 0.006–0.017 (7) | Weekly ship CTD rosette samples 9th Jan to 10th Feb |
| Ridge ice | 0.28–3.03 (11) | HAVOC study ridge keel samples 10th Jan (9) and 24th Jan (2) |
| Ridge void | 0.001–0.031 (6) | HAVOC study ridge keel void on 10th Jan (3) and 24th Jan (3) |
| Level ice 1 | 0.15–3.61 (10) | Level ice on one side of study ridge on 3rd Jan |
| Level ice 2 | 0.12–1.37 (7) | Level ice on other side of ridge on 3rd Jan |

The number of samples included is shown in parentheses. See Fig. 2 for sampling sites at Fort Ridge, the HAVOC-MOSAiC study ridge.

**Table 2 | Abundance and biomass of tintinnids, dinoflagellates, heterotrophic nanoflagellates and bacteria and bacterial production below the sea ice**

| Organism | Abundance[a] (cells L$^{-1}$) | Biomass[a] (ng C L$^{-1}$) | Production[a] (ng C L$^{-1}$ d$^{-1}$) | Sampling depth below ice (m) | Sampling dates (dd.mm.2020) |
|---|---|---|---|---|---|
| Tintinnids[b] | 14.7 ± 2.7 (4) | 44 ± 8 | | 1 1 and 10 1 | 25.01 02.02 08.02 |
| Dinoflagellates[b] | 19 ± 4·10$^3$ (6) | 896 ± 140 | | 0.01, 20 [d] 20 2[e] | 18.01 22.01 24.01 |
| Flagellates[c] | 90 ± 11·10$^3$ (3) | 850 ± 17 | | 20 | 23.01 30.01 07.02 |
| Bacteria[c] | 134 ± 3·10$^6$ (3) | 2940 ± 147 | 49 ± 1.5 (3) | 20 | 22.01 23.01 30.01 07.02 |

Samples for tintinnids (*Ptychocylis obtusa)* were collected using a plankton net attached to a remotely operated vehicle (ROV). Samples for dinoflagellates were collected with a ROV suction pump close to the ice underside and from 20 m depth at Fort Ridge, with a bilge pump (Supplementary Fig 1A) from internal void in Fort Ridge, and with a Niskin bottle on Jan 22. from 20 m depth at Ocean City. For flagellates and bacteria samples were collected with Niskin bottles attached to the ship CTD rosette on RV Polarstern. See Fong et al[25]. for a map of the sampling sites in the MOSAiC Central Observatory. [a]average ± SE, number of samples in parentheses, [b]microscopy counts, [c]flow cytometry counts, [d]sampled with suction pump close to ice underside and from 20 m depth at Fort Ridge, [e]sample from ridge keel void.

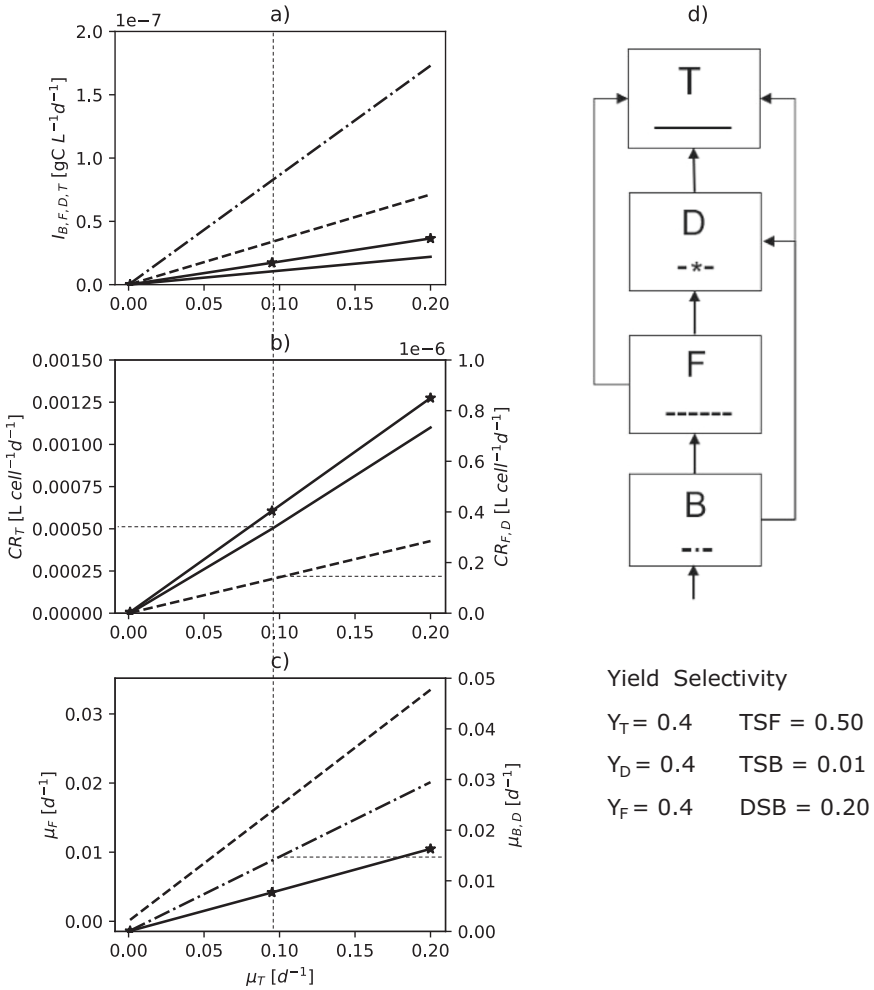


**Fig. 4 | Carbon flow, clearance and growth rates as function of tintinnid growth. a** Carbon demand for the trophic levels as a function of tintinnid growth rate calculated with the steady state Eqs. 1–3. **b** Clearance rates (CR) for the predators as a function of tintinnid growth rate derived from the carbon demand (Eq. 4). **c** Growth rates for the functional groups as a function of tintinnid growth rate (Eq. 5). **d** Schematic of the flow of carbon through the trophic levels of the microbial food web. In each box the line style for each group that is used in a-c. The calculations are based on measured biomasses for each trophic level shown in Table 2. The trophic levels are B: heterotrophic bacteria, F: heterotrophic nanoflagellates, D: heterotrophic dinoflagellates, T: tintinnids. Sensitivity analysis was performed for all model parameters (Yield and Selectivity for prey) and results are shown in Supplementary Figs. 3 and 4.

(Supplementary Fig. 1) which have been shown to feed on cyanobacteria with similar size as heterotrophic bacteria. According to Strom[41] however, there is a threshold level for bacterial biomass concentration of 20 µg C $L^{-1}$ below which the dinoflagellates ingested little bacteria. In our case, the concentration of B was 3 µg C $L^{-1}$ (Table 2), i.e., far below this threshold and even if we set the selection for bacteria at maximum in our steady state food web, the calculated $CR_F$ would still amount to almost double the theoretical maximum, in order to provide enough carbon to higher trophic levels in the model.

To conclude, the steady state model indicates that pelagic bacterial production alone could not supply all the organic carbon to maintain the microbial food web we observed with tintinnids as top predators, because of a bottleneck in the carbon transfer at the level of bacterivorous flagellates.

### Can organic matter inside sea ice become available to pelagic protists during the polar night?

The only place where we recorded a substantial amount of biomass with a potential to serve as an additional food source at this time of the year, was within sea ice (Table 1). We observed internal algal biomass layers in level ice at both sides of the studied ridge (Fig. 5) as well as in ice cores from the first-year ice (FYI) coring site (Supplementary Fig. 5). As described above, such layers consist of protists and other organic matter trapped in the ice during the previous growth season[14,15]. We suggest that sea-ice deformation and warming during ridge formation might provide a mechanism whereby this material can become available to protists in the under-ice water column.

The brine volume fraction (BVF) of sea ice determines its microporosity and permeability and is a function of temperature and bulk salinity[42]. With BVF > 5% the brine channels are connected, i.e., sea ice is considered permeable, and brine percolation is possible with exchange of brine and biomass across the ice-water interface. At low temperatures the BVF decreases[17], and the material trapped in the brine channels gets locked in the ice. In the level ice adjacent to the ridge the BVF was lower than 5% down to below the algal layer (Fig. 5a, b), i.e., this biomass was located in the impermeable part of the level ice during the winter which reduces the possibility of this material to be released from the ice. We have previously suggested that algae are released from the ice in spring due to warming of the ice[15]. Here we argue that some material can also be released in winter during ice deformation and the formation of sea-ice ridges or rubble. When sea-ice ridges form, ice blocks are submerged forming the ridge keel (Fig. 2). Once submerged the ice blocks would reach the same temperature as the surrounding seawater. A big part of the keel (below the consolidated layer) had a temperature close to the seawater temperature of −1.8 °C, i.e., the freezing point of seawater, and thus a BVF » 5% (Fig. 5c). The combination of higher BVF after the mechanical breakup of the level ice and submerging of ice blocks during ridge formation may allow release of material from the ridge keel ice blocks to the under-ice water. During our ridge keel coring in January, we observed soft, slushy, and porous ice warmed up to the seawater freezing temperature, from 2 m depth downwards (Fig. 2).

We have several observations supporting our hypothesis that algae and other organic matter are released to the water column in winter during ridge formation. Firstly, the similarity of the aggregates of algae and organic matter in the ridge ice, level ice and the under-ice water column studied by light and scanning electron microscopy (SEM) (Supplementary Figs. 2, 6 and 7). These included silicoflagellates, typical sea ice diatoms like *Nitzschia frigida* and *Fragilariopsis* sp., and resting cysts, mainly from chrysophytes and dinoflagellates. Secondly, the community composition of

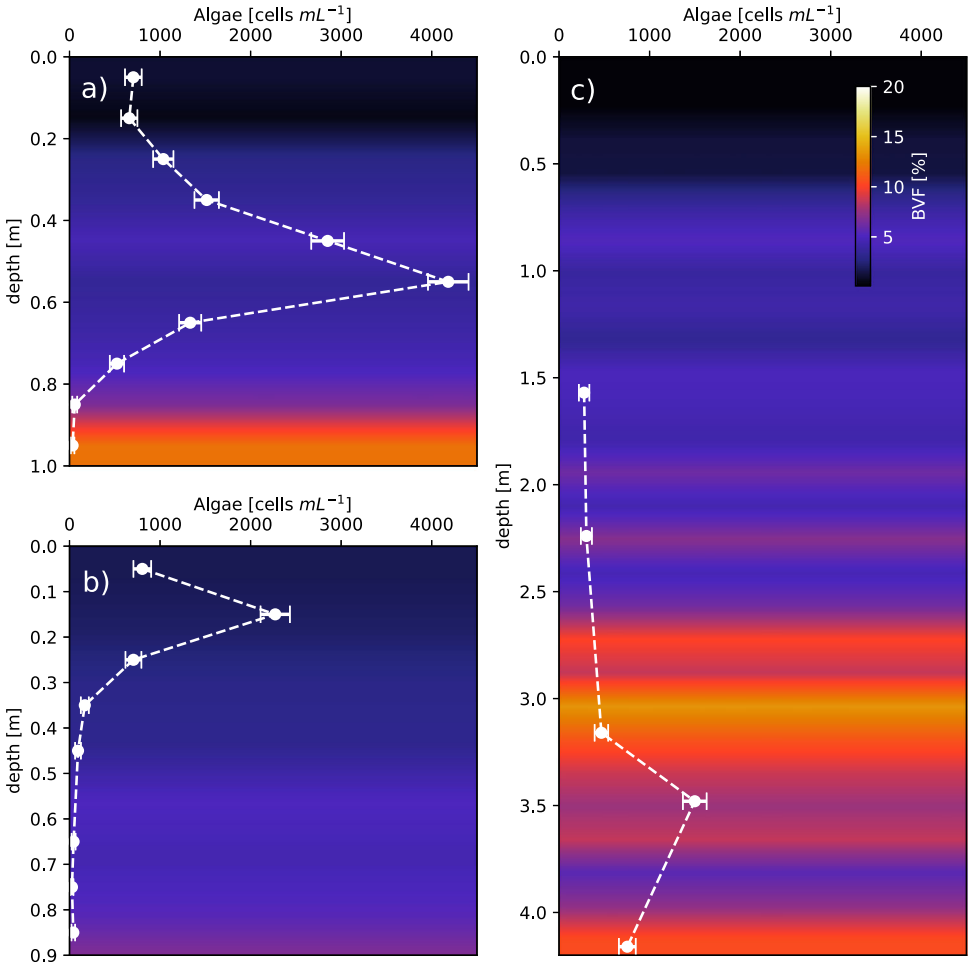


**Fig. 5 | Brine volume and algal abundance in ice core profiles. a**, **b** First-year level ice cores from both sides of Fort Ridge. **c** Ridge keel ice core. Color show brine volume fraction (BVF, color scale in c) and white dashed lines show algal abundance. Error bars are counting precision calculated as the 95% confidence limit. The range of chlorophyll a (photosynthetic pigment) for the profiles in (**a**–**c**) are given in Table 1 as Level ice 1, 2 and Ridge ice, respectively.

protists and bacteria seen from 18S and 16S gene profiling suggests that the species composition in the water column at 20 m depth was similar to the species composition in first-year sea ice (Supplementary Fig. 8). The ROV suction pump sample taken directly at a ridge ice block with visible brownish aggregates had a much higher abundance of protists, especially diatoms, than samples taken from the bottom of level ice or from the water column (Supplementary Fig. 1), which indicates the potential for material being released due to increased porosity because of increased ice temperature after ridging. Because the ice cores from the ridge were melted without seawater addition due to the need to also take salinity samples from the same cores, the osmotic shock during melting may have resulted in an underestimation of biomass and biodiversity in these samples[43,44].

Interestingly, as tintinnids have a food size preference of 20–30% of their lorica oral diameter (LOD)[39,45], and we measured a mean LOD of *Ptychocylis obtusa* of 56 µm ($n = 10$) suggests that their optimal food size is 12–18 µm, which is larger than bacterivorous flagellates, typically with a diameter of around 5 µm[2], leaving only the dinoflagellates as an optimally sized prey. However, a large part of the presumably sea ice originating particles we found in the water column were in the size range 10–40 µm (Supplementary Fig. 9). Most of the dinoflagellates were 10–20 µm (Supplementary Fig. 1), but *Gymnodinium* sp. can feed on particles their own size[34,46], so it is possible they also exploited the sea-ice food source, and themselves were a food source for the tintinnids. Dolan et al.[29] observed that the abundance of tintinnids in the western Arctic Ocean was an order of magnitude lower in open waters in August 2011 compared to ice-covered waters in August 2012. The tintinnid community in 2012 was composed of species with larger LOD, including *Ptychocylis* sp., i.e., they preferred larger prey than those dominating in 2011. The authors proposed that the phytoplankton community associated with the summer sea ice was distinct from the one in the ice-free year and thus influenced the tintinnid community composition. It is possible this reflects a similar release of food particles from the ice as we propose for winter, only here consisting of a more active ice algal community in summertime.

### Plausibility of a winter food web supported by ridge formation

We were not able to directly measure the release of particles from the ice following ridge formation. To check the plausibility of our hypothesis we created a theoretical scenario based on our observations and scientifically justified assumptions. The first two main events of the scenario are outlined in Fig. 6.

As a starting point for our estimate of the dispersal of the particles in the water column we assume they are released in the immediate vicinity of the ridge keel (Fig. 6).

With the dispersal rate we obtained from the Lagrangian simulation with Open Drift (Supplementary Fig. 10), with spread of particles (m) = 774t + 0.02 ($R^2 = 0.97$), where t is time (days), we calculated the area increase of the patch (Fig. 7a). With the sinking rate set to 1 m $d^{-1}$ as an approximate average value for organic particles[47] in the size range of interest (diameter 2–40 µm) we obtained a formula for patch volume (PV) increase by fitting a polynomial function:

$$PV_t = 38.7t^2 + 39.7t + 1 \quad (6)$$

where t is time (days) and $PV_{t0}$ is set to 1 L for the convenience of further calculations. We then use this to calculate the particles per volume as a function of time in the patch (Fig. 7b).

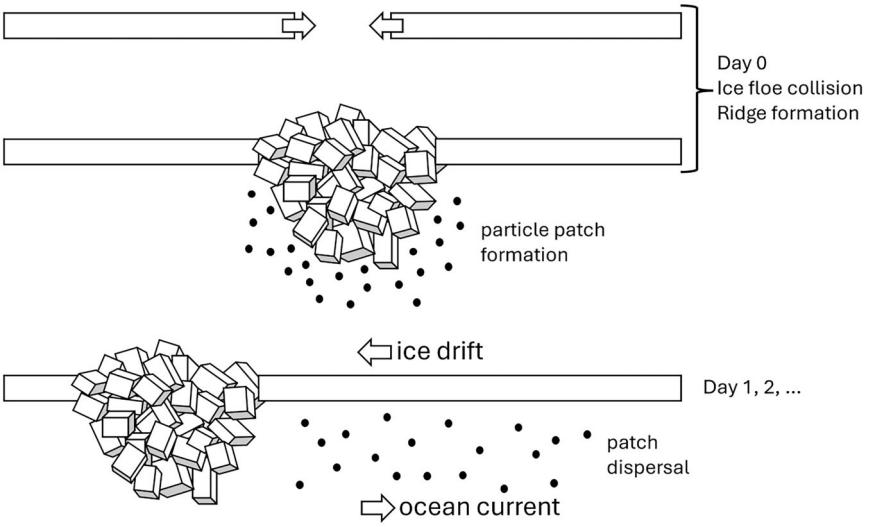


**Fig. 6 | Ridge formation and particle patch formation.** Schematic illustrating the sequential steps of sea-ice ridge formation, particle patch formation and particle dispersal in the water column. Ice drift and ocean current can have any direction relative to each other horizontally.

Our question is whether these patches of food particles can sustain the tintinnids. We describe the change in tintinnid abundance with the equations:

$$(T/L)_t = (T/patch)_t/PV_t \quad (7)$$

$$(T/patch)_t = ((T/patch)_{t-1} x GR) + TB_{t-1} \quad (8)$$

$$(TB)_t = (PV_{t+1} - PV_t) x (T/L)_{t0} \quad (9)$$

where T/L is tintinnids per liter, PV is patch volume (L), t is time (days), TB is the background tintinnid abundance in the patch (tintinnids per patch), GR is growth rate ($e^r$), and r is specific growth rate. For the calculation we set TB to the abundance we observed so that $(T/L)_{t0} = 14.7$ (Table 2), and $(T/patch)_{t0} = 14.7$ when we set $PV_{t0} = 1$ L. The specific growth rate (r) is a function of food particle concentration[38]:

$$r = (r_{max}(P-P'))/(k + P-P') \quad (10)$$

where $r_{max}$ is the maximum growth rate, set to 1 $d^{-1}$ for tintinnids[38], P is the particle concentration, P′ is the minimum particle concentration that can sustain growth, and k - P' is homologous to the half saturation constant in saturation kinetics. We set P′ to 1 ng C $mL^{-1}$[38].

We observed an abundance of tintinnids of 14 ± 2.7 cells $L^{-1}$ over a period of 14 days (Table 2) during a drift of 0.9–11 km, on average 6.3 ± 0.9 km (avg. ± SE) per day, and in total 88.1 km (Fig. 1). This suggests that the geographical distribution of the population could be at least in the order of hundred kilometers. Can patch formation by ridging sustain tintinnids over a large area for a long period? We approach this question with an idealized ridge model that corresponds approximately to the ridge properties measured during MOSAiC [48] with a keel width of 30 m (Supplementary Fig. 11) and, according to typical first-year ice ridges, a keel depth of 7 m and a macroporosity of 30%[49,50].

The 30-day running mean of convergence observed within 5 km around the MOSAiC ice floe from Sentinel-1 Synthetic Aperture Radar (SAR) satellite, suggests that on average 1% of the ice area was consumed by ridge formation each day in December and January[51]. While we are aware that deformation has an intermittent character, we use this simplified approach of a mean daily deformation rate for an idealized model setup. Given the assumption on the size and porosity of the ridges stated above, this results in the daily loss of 1 $km^2$ level ice in a 100 $km^2$ area, because a 30 m wide ridge keel need ice from an approximately 100 m wide area (Supplementary Fig. 11). For our scenario we let the ridge form as a straight line which cross a quadratic 100 $km^2$ area perpendicularly (Fig. 7a). Sea ice typically deforms along long lines (linear kinematic features) which can extend for hundreds of kilometers[51,52].

Using Eqs. 7–10 we can calculate how much particulate carbon must be released during ridge formation to maintain the tintinnid abundance above the initial concentration until an area is covered by the patches, i.e., a semi stable abundance. We set the area to 100 $km^2$ because this matches approximately the area on which deformation rates were measured by satellite, as well as the area of our tintinnid observations. With 1 patch forming every day this would take 4.5 days according to our estimated dispersal rate (Fig. 7a). Then, the needed initial carbon concentration immediately after release is 347 mg C $m^{-3}$ (Fig. 7d). To our knowledge there are no published studies on the release of particles from sea ice during ridge formation. As a first approach we assume that for particles to be released the ridge ice blocks should first become permeable, i.e., reach a temperature close to that of the surrounding seawater. We use a simple analytical solution of when ice blocks reach seawater temperature depending on block thickness [53] which was validated in the laboratory [54]. When the temperature in the center of an ice block approaches the seawater temperature, it is in thermal equilibrium (Fig. 7c). Then, assuming that the part of the ice block that reached seawater temperature during ridge formation released all its particles due to increased permeability and possibly due to increased turbulence inside the ridge [55], the amount released depends on the concentration in the ice and the total ice volume warmed up.

According to our measurements in level FYI cores from the MOSAiC ice floe from the period of this study, the average concentration of particulate organic carbon (POC) was 276 ± 24 mg C $m^{-3}$ (Supplementary Fig. 5). We simplify and assume the POC was evenly distributed in the ridge keel ice. Since the level ice blocks forming the ridge were randomly broken up and assembled into the keel this should be a reasonable approximation. To have a starting concentration for the particle patch we defined that immediately after ridge formation all particles were released into a zone of about 1 m depth under the ridge keel, so that under 1 $m^2$ of sea ice there was one $m^3$ volume of water into which the particles are released initially. Then, under a 1 m thick slice of the ridge keel which is 118 $m^3$ with a surface width of 30 m, there was a 30 $m^3$ water volume receiving the particles from the slice (Supplementary Fig. 12). In order to have an initial concentration of 347 µg C $L^{-1}$, 12 % of the ice blocks in the keel must have reached the seawater temperature and released its particles, i.e., 12 cm into a 1 $m^3$ cubic ice block from all sides. According to the thermodynamic model this process would take about 2 h (Fig. 7c), whereas after 0.5 or 1 h the carbon release would be sufficient for maintaining abundance above the initial for 3.5 and 4 days, respectively (Fig. 7d). We know from observations during the MOSAiC expedition that ridges can form in a few hours, thus the almost instantaneous release of up to 347 µg C $L^{-1}$ appears to be possible, although

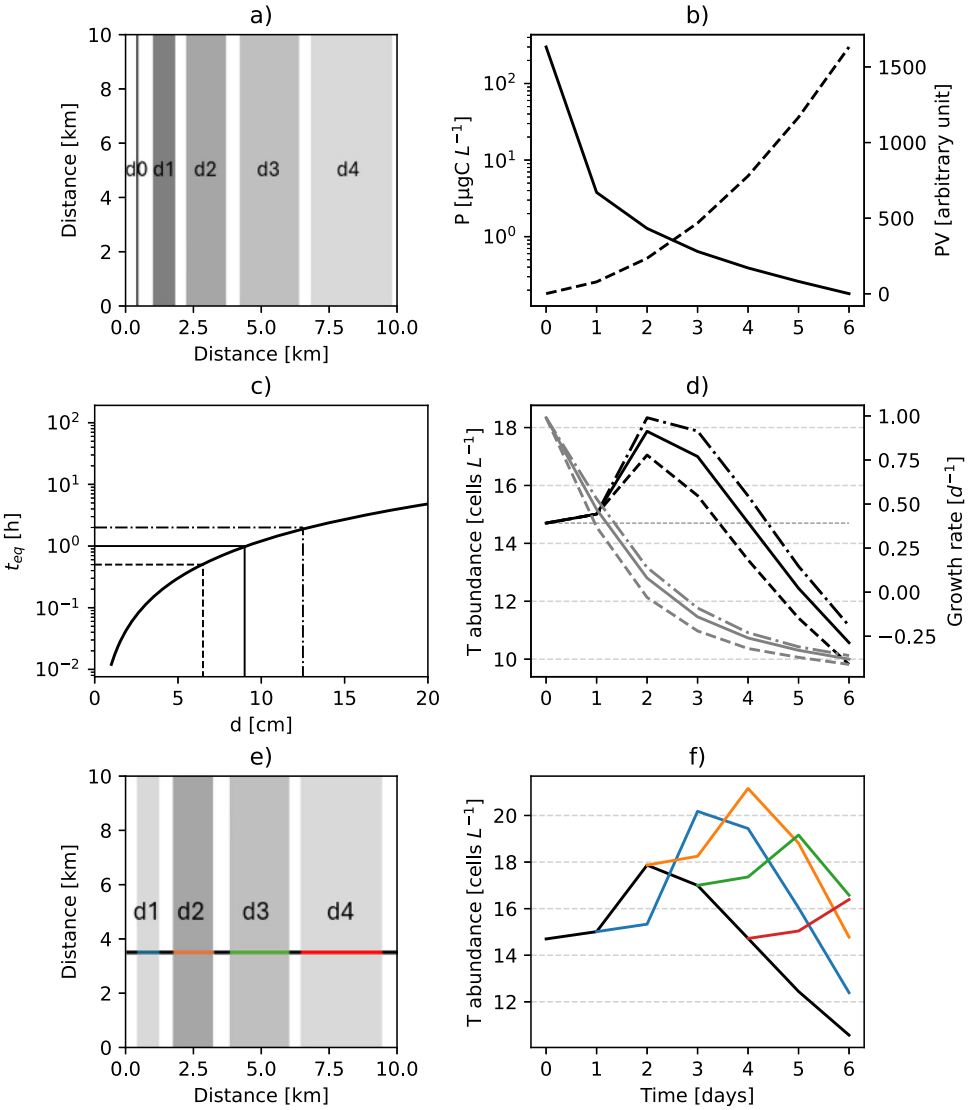


**Fig. 7 | Particles patch formation and tintinnid growth. a** Increase in patch area with time (days, d1-d4) starting with linear patch stretching over the entire 10 km length across, with the expansion rate derived from Lagrangian dispersal simulation (Supplementary Fig. 10). **b** Particle patch volume from Eq. 6 (PV, dashed line), and particle concentration (P, solid line), i.e., dilution by dispersal, as a function of time. **c** Analytical solution (curved line) of time before ice blocks reaches seawater temperature ($t_{eq}$) depending on block thickness (d) according to refs. 53, 54. Straight lines show thickness of ice warmed to seawater temperature after 0.5 (dashed), 1 (solid) and 2 (dash dot) hours. **d** Change in protist growth rate (grey lines) and abundance (black lines) with time after particle patch formation for three initial concentrations of released particles following the three indicated release times from warming of the ice in c (217 (dashed), 293 (solid) and 347 (dash dot) µg C/L). **e** Shading indicates tintinnid concentration in the patch on day 1-4 (d1-d4) with the highest concentration on day 2. Color of horizontal line indicates new patches formed perpendicular to the other, older patches. **f** Effect of new patches forming over the original patch on the growth of protists. The black line is the tintinnid concentration in the original patch and colored lines show tintinnid growth in patches forming over older patches as indicated with the respective colors in e.

the longer the time the less instantaneous the release. The concentration of the food patch decreases relatively fast, and a positive growth rate is sustained for 1.5–2.5 days (Fig. 7d). Because of the fast dispersal of particles, tintinnid consumption has very little impact on the particle density. However, with the release of patches of particles over older patches, the population of tintinnids can reach a higher peak concentration, and the period with an abundance above the initial abundance is prolonged. This is mainly due to the higher initial abundance of tintinnids (Fig. 7e, f).

To evaluate our assumptions on the ridge formation in the idealized model, we compared the ridged ice area fraction with observations from the surroundings of the MOSAiC floe using ICESat-2 satellite altimeter data (see Methods). For the location of the MOSAiC ice floe, the ICESat-2 ridge spacing decreased from 460 m in October to 160 m in May (Supplementary Fig. 13A). Assuming a ridge width of 36 m [49], this gives an increase of ridge areal fraction from 8 % in October to 22 % in May (Supplementary Fig. 13C). This estimate corresponds to an average increase of ridge area by 2.3 % per month [56]. The 1% of the area converging every day we used for our model would give an increase of about 9% per month. This discrepancy could be in part because all convergence might not form ridges but rather rubble fields and rafted ice. The SAR data shown by refs. 51, 57 indicates that these convergence events were intermittent, with a few days with convergence up to 10% followed by quiet periods of a few days. Thus, if the release from the ice was the only food source for tintinnids, one should probably expect a larger variation in the abundance than our model simulation indicates. But if we also take into consideration that the microbial food web could deliver about 1/3 of the carbon demand of the tintinnids (Fig. 4), the two sources combined should be sufficient to maintain a stable population.

Satellite observations show that ridge formation is abundant arctic-wide [56], and this is also evident of direct observations of Arctic ice draft from sonars[22,58,59]. Direct observations at three sites in the Beaufort Gyre pack ice over a full year, indicated that ridge keel areal fraction was about 30% (Brenner et al., 2021), suggesting that ridge fraction during MOSAiC was representative for the Arctic Ocean. Accordingly, the mechanism we have described may apply to the entire pack ice region of the Arctic Ocean.

## Conclusions

Neither the microbial food web fueled by bacterial production, nor the release of organic matter from the sea ice during ridge formation alone was sufficient to explain the stable presence of an active population of tintinnids we observed in the Arctic Ocean during the polar night. However, combined these two food sources were enough. In addition, it is also possible that the released organic matter was a food source for dinoflagellates, flagellates and bacteria, giving short transient boosts to the microbial food web.

We present evidence that material from the sea ice was indeed present in the water column and that this mechanism appears to be important in maintaining active populations of planktonic protists through the polar

night. Our upscaling exercise based on observed ridge formation rates suggests that such release of food particles can supply extra energy during the polar night to the pelagic food web in the entire Arctic Ocean. It follows from this that the predicted ice-free summers in the Arctic Ocean due to global warming[60], may have implications for the protist community at the base of the food web, because the winter food reservoir in the sea ice will be very much reduced if there is no sea ice to accumulate it during the most productive summer period[15,61].

## Methods

### Study area

This study was conducted in the central Arctic Ocean during leg 2 of the Multidisciplinary drifting Observatory for the Study of the Arctic Climate (MOSAiC) expedition when the research vessel RV *Polarstern* was drifting with an ice floe from 86.6 °N, 118.4°E on December 13, 2019, to 88.6°N, 61.3°E on February 23, 2020 (Fig. 2) in the eastern Amundsen Basin[24].

The sampling for this study was performed entirely on or from the MOSAiC ice floe in the first central observatory (CO1)[25]. The oldest ice of the floe was formed shortly after freeze-up in 2018[62]. A sea ice ridge observatory (SIRO) was established in late December 2019 at a ridge on the MOSAiC floe named Fort Ridge. The ridge keel was approximately 100 m long and 20–30 m wide (Fig. 2 and Supplementary Fig. S11). The ridge was formed from 0.1–0.8 m thick blocks, most likely during October 2019[63] and its average sail height was 1.5–2.0 m. The maximum sail height was 2.7 m, while the maximum keel depth was 6.4 m. Ridge ice salinity (practical salinity, dimensionless) was 3.9 ± 1.8, while the bulk salinity of adjacent 0.9–1.0 m thick level ice was 4.1 ± 1.2 and 4.8 ± 0.4 on either side of the ridge.

### Water sampling with Remotely Operated Vehicle (ROV)

Abundances of plankton were estimated based on samples collected with a plankton net mounted on an underwater remotely operated vehicle (ROV). The ROV used in this study is described in Katlein et al.[64], and a general description of the ROV biological sampling during MOSAiC is found in Anhaus et al.[65] and Fong et al.[25]. During the period 25$^{th}$ January to 8$^{th}$ February four horizontal net hauls were performed providing samples for plankton analysis. The net hauls were taken with a nylon net with a rectangular opening of 10 × 15 cm and a mesh size of 30 µm [66]. The net was mounted on the ROV and towed in a horizontal transect at a depth of 1 m below the sea ice, and at 2$^{nd}$ of February at both 1 and 10 m depth, after which the sample was taken from the cod end of the net. During the net tow, the ROV was moving steadily at a speed of 0.1–0.2 knots. To estimate the volume of water that passed through the net, we used the area of the net opening combined with the length of the net tow transect calculated from the speed and time of the transect. For ROV suction sampling at Fort Ridge a Sea Bird low-speed suction pump was attached to the ROV, and the samples were collected through a 1 cm diameter silicone tube protruding at the front of the ROV enabling simultaneous observation with the ROV front camera. One dive mission with suction sampling at four sampling points at Fort Ridge was performed on 18$^{th}$ of January 2020: 1) on the surface of a ridge keel ice block with brownish material assumed to be algae, 2) in a crevice between two blocks of ice near the bottom of the ridge keel, 3) on the bottom surface of level ice close to the ridge, and 4) in the water column at 20 m depth.

### Sampling of ice and water from ridge and level ice

Ice coring was performed at Fort Ridge, both on level ice on both sides of the ridge and in the ridge keel (Fig. 2). Additional ice coring was performed weekly at the designated MOSAiC first-year ice (FYI) coring site[24,25]. Ice cores from ridge and level were extracted with KOVACS Mark II coring system with 9 cm inner diameter. For the MOSAiC main coring program, the ice cores were sectioned and treated further for various sub samplings according to Nicolaus et al.[24] and Fong et al.[25]. In short, 3–4 cores were pooled per depth section and melted with addition of 0.2 µm filtered seawater (50 mL for each 1 cm of core to give a final salinity of approximately 20) to reduce osmotic shock and microbial cell loss[43,44,67]. Core sections for nutrient samples were melted without addition. The ice core and water samples extracted specifically for this study are described in the following. Three missions to Fort Ridge for biological sampling from level ice, ridge ice and water from water-filled ridge keel voids were performed during January 2020. On Jan 3$^{rd}$ three replicate cores were sampled on level ice close to the ridge on both sides (Fig. 2). The whole cores were cut into 10 cm long sections. For biology-related sampling, the three replicate core sections were pooled to have sufficient volume for subsampling. These core sections were melted without adding filtered seawater (final salinity approximately 4) in order to secure samples for salinity measurements because of the difficult conditions for coring the ridge during the winter conditions. Samples for protist counts by light microscopy, flow cytometry (FCM) counts of bacteria and protists, chlorophyll a (Chl a), scanning electron microscopy (SEM), nutrients and salinity were collected from the melted ice sections. The measurement of particulate organic carbon (POC) in the sea ice used for our estimation of POC release from the ice during ridge formation was from the MOSAiC main coring and therefore with buffered melting. We do recommend melting ice cores with added seawater for biological samples.

The first coring of the ridge keel at Fort Ridge was performed on January 10$^{th}$. The sampling point was close to the middle of the ridge sail (Fig. 2). Two cores through the ridge keel were extracted. On Jan 24$^{th}$ a second coring with extraction of one core of the ridge keel was performed at a site approximately 8 m away from the Jan 10$^{th}$ coring site. The cores were packed individually in plastic bags, brought to the ship and stored at −20 °C until sections were cut for sub-sampling in a cold lab onboard. The sections were melted without addition of seawater and samples were taken for bulk salinity and the biology-related variables as listed for the level ice cores above. Since voids in the ridge keel had been detected during coring, water from one selected water-filled void on each coring mission was pumped with a manual bilge pump with a silicon tube with diameter 20 mm into pre-washed polyethylene containers.

Ice cores for measuring sea-ice temperature were taken weekly at FYI and SYI sites[68,69]. A full-length core was extracted, and temperature was measured with a temperature probe in holes drilled every 5 cm from top to bottom. In the ridge, temperature was monitored using three ice mass balance buoys deployed through the ridge keel[70,71]. They were set up in early January, i.e., at the beginning of our observations (Fig. 2). Ridge temperature from buoys and level ice temperature measured manually from ice cores, along with salinity measurements, were used to calculate the brine volume fraction (BVF) of the level ice and ridge keel ice following Cox and Weeks[42].

Samples of under-ice water were taken with Niskin bottles attached to a CTD rosette on the on-ice operated CTD at the Ocean City (Jan 22) site on the MOSAiC floe[72] and with the ship CTD weekly on Polarstern. For this study samples were taken at 20 and 1000 m depth below ice (Fig. 2).

### Flow cytometry

Subsamples for flow cytometry were prepared by filling triplicate cryotubes with 1.8 mL of the sample. The samples were fixed with glutaraldehyde at a final concentration of 1% at 4 °C in the dark for 2 hours and then flash frozen in liquid nitrogen and stored at −80 °C until analysis. Bacterial abundance was determined with a FACS Calibur (Becton Dickinson, San Jose, Calif. USA) flow cytometer. The fixed samples were diluted with 0.2 µm filtered TE buffer (Tris 10 mM, EDTA 1 mM, pH 8), stained with the fluorescent nucleic acid dye SYBR Green I (Molecular Probes, Oregon, USA) and incubated for 10 min at 80 °C[73]. The stained samples were counted with a flow rate of approximately 60 µL min$^{-1}$. Gating was applied on bi-parametric plots of green fluorescence vs. side scatter as described in Marie et al.[73] to discriminate bacteria from other particles (Supplementary Fig. 14). Abundance of bacteria were converted to carbon biomass with 20 fg C per cell[74]. Heterotrophic nanoflagellates (HNF) were counted with an Attune® NxT, Acoustic Focusing Cytometer (Thermo Fisher Scientific) with a 20 mW 488 nm laser. The cells were stained with SYBR Green I (Molecular Probes, Oregon, USA) and quantified according to the protocol of Zubkov et al.[75], (Supplementary Fig. 15). The biomass was calculated from equivalent spherical diameter (ESD) and the conversion factor of Børsheim and Bratbak[76].

### Light microscopy

Protist samples were filled in 200 mL amber glass bottles and fixed with 25% glutaraldehyde and 20% hexamethylenetetramine-buffered formaldehyde solution to final concentrations of 0.1% and 1% (vol/vol), respectively. The samples were kept at 4 °C in the dark until the cells were identified and counted by light microscopy. For microscopy counts the cells were settled in Utermöhl sedimentation chambers (HYDRO-BIOS©, Kiel, Germany) for 48 h and identified and counted in an inverted light microscope (Nikon Ti-U). A minimum of 50 cells of the dominating species were counted, giving a maximal count uncertainty of ± 28% [77]. In addition, unfixed samples of 3 or 10 mL from melted ice cores and seawater samples were settled in Utermöhl sedimentation chambers onboard Polarstern and examined in a Nikon TS100 microscope. Cell abundance was converted to carbon biomass from biovolume [78] with published volume to carbon conversion factors[79].

### Scanning electron microscopy

Samples for scanning electron microscopy (SEM) were collected by filtering seawater samples and melted ice samples onto 0.6 µm polycarbonate filters with a 47 mm diameter, which were air dried and stored inside 50 mL polyethylene falcon tubes until analysis. Sub samples of the dried filters were attached to aluminum stubs with carbon tape and coated with gold/palladium before examination and imaging in a FEI Quanta 450 or a Zeiss Supra 55 VP scanning electron microscope. After the scale of the SEM image was set, the particles on the filter were detected and counted by manual thresholding and the particle analysis routine in the image analysis software NIH ImageJ. All particles detected with a major axis < 10 µm were removed from the analysis because it was difficult to differentiate between particles and the structure of the filter at the magnification used (Supplementary Fig. 7).

### Chlorophyll a

Seawater and melted sea-ice samples for chlorophyll a (Chl a) were filtered on 25 mm GF/F filters using mild vacuum (Whatman). Chlorophyll a was extracted in 90% acetone for 12 h at 5 °C and measured with a Turner 10 AU Fluorometer (Turner Design, Inc.). Phaeopigments were measured after acidification with 5% HCl[80].

### Particulate organic carbon (POC) concentrations in the sea ice

Melted sea ice was filtered on pre-combusted Whatman GF/F filters with low vacuum pressure ( ≤ 30KPa), freeze dried and carbonates were removed by contact with HCl fumes for 4 h in a vacuum-enclosed system. Filters were packed into tin cups and analyzed with an elemental analyzer (Flash 2000, Thermo Scientific, Milan, Italy) at the University of La Rochelle, France (Littoral, Environment and Societies Joint Research Unit stable isotope facility).

### DNA extraction, PCR and Illumina 18S and 16S sequencing

Water samples (250–500 mL) from 20 and 1000 m depth (10.02.2020), from a water-filled void inside the ridge (at 204–224 cm below the ice surface; 24.01.2020), a horizontal net tow (08.02.2020) and melted sea ice samples from FYI (50–80 cm, 03.02.2020), SYI (60–70 cm, 70–80 cm, 80–93 cm; 13.01.2020) and ridge ice above and below the water-filled void (157–204 cm; 224–260 cm; 24.01.2020) were filtered onto a 0.22 µm Durapore® Membrane Filter (Ø 47 mm, Merck-Millipore) and the filters transferred into 2 mL cryovials and stored at −80 °C until analysis.

DNA was extracted from the filters using the DNeasy Power Soil Kit (Qiagen), following manufacturer's instructions and the extracted DNA was stored at −20 °C until PCR amplification (two-step nested PCR approach using HotStarTaq Master Mix (Qiagen) for the bacterial/archaeal 16S rRNA gene [519 F: CAGCMGCCGCGGTAA[81]; and 806RB: GGACTACNVGGGTWTCTAAT[82]; and for the eukaryotic 18S rRNA gene [EukA7F: AACCTGGTTGATCCTGCCAGT[83]; and Euk570R: GCTATTGGAGCTGGAATTAC[84];. For the first PCR, conditions were as follows: initial denaturation of 15 min at 95 °C, followed by 25 cycles of 95 °C for 20 s, 55 °C for 30 s, and 72 °C for 45 s and a final extension step of 72 °C for 7 min. The second PCR was done to add unique eight-nucleotide barcodes to the first PCR products with following PCR reaction conditions: initial denaturation of 15 min at 95 °C, followed by 12 cycles of 95 °C for 20 s, 62 °C for 30 s, and 72 °C for 30 s, followed by a final extension step of 72 °C for 7 min. The final PCR products were purified with Agencourt AMPure XP magnetic beads (Beckman Coulter Inc., CA, USA), quantified using Qubit 3.0 Fluorometer and pooled in equimolar concentrations and sequenced at the Norwegian Sequencing Center (Oslo, Norway) using the MiSeq Reagent Kit v3 (Illumina, CA, USA). The sequencing data is available at the European Nucleotide Archive (ENA) under study accession number PRJEB75226. A total of 10 samples were analyzed for 16S and 18S community composition and the retrieved sequence data (16S: 293568 reads and 18S: 397804 reads) was processed using the R package DADA2 (Divisive Amplicon Denoising Algorithm 2, version 1.2.4[85]; in R (version 4.2.2[86]). For this, sequences were trimmed, filtered based on quality scores, dereplicated and amplicon sequencing variants (ASVs) inferred. For 16S sequences, both forward and reverse reads were denoised and merged before chimeric sequences were removed, while for 18S data, due to bad quality of the reverse read, only the forward read was used for analysis. Taxonomy was assigned using the 16S silva database (version 138)[87] and the 18S pr2 database (version 4.12.0)[88]) for 16S and 18S sequences, respectively. For ordination analysis (multidimensional scaling, MDS), Bray-Curtis dissimilarity was calculated based on relative abundance data (square-root transformed) of all ASVs for both 16S and 18S rDNA gene sequences using the R package vegan.

### Bacterial production

Bacterial production was estimated from the incorporation of $^{3}H$ labeled leucine according to the method of Smith and Azam[89]. 1.5 mL subsamples were incubated in triplicate with added [$^{3}H$]leucine (3.93 TBq/mmol) at a final concentration of 50 nM for 10 hours in the dark at 1 °C in an incubator onboard. For each sample one control was prepared in the same way but metabolic activity was stopped by addition of 100% trichloroacetic acid (TCA) to a final concentration of 5% before the addition of [$^{3}H$]leucine. The incubation of the triplicates was stopped with TCA in the same way as for the control. The bacteria were harvested from the samples by centrifugation and washed with TCA according to Smith and Azam[89]. Scintillation cocktail (Ultima Gold) was added before incorporated $^{3}H$ was measured in a Packard Tri-Carb scintillation counter.

### Simulation of particle patch dispersal in the water column

To estimate the horizontal spreading of a particle patch released from ridged ice we performed Lagrangian simulation in the modeling environment Open Drift[90] with a modified version of the Pelagic Egg Drift model. The simulation was performed with 2000 particles, each with a cell diameter of 20 µm. They were set to be neutrally buoyant in order to simulate only the horizontal spread of particles of a size representative of the particles released from the ice. Turbulence was modeled in Open Drift parameterized according to a random walk model as explained in Dagestad et al.[90]. The starting point of the particle patch, representing organic matter released by the formation of a pressure ridge, was set at 5 m depth with a 50 m radius. For the simulation we used the average current speed measured under the sea ice at 20 m depth during January and February 2020 of 3–5 cm $s^{-1}$[91]. Environmental variables used in the simulation were sea floor depth, salinity, sea water temperature, x and y sea water flow in the location from Topaz4[92], and x and y wind speed from MEPS (MetCoOp Ensemble Prediction System). From the simulation the latitude and longitude vs. time were used to calculate the distances from the origin with the Haversine formula, and from the geometric center at each time step for the simulated particles (Supplementary Fig. 10). The spread distance was defined as the standard deviation of the distances from the geometric center at the final time. From the Stokes equation with spherical particle diameters of 2–40 µm, sea water density 1.025 g $cm^{-3}$, particle density 1.085 g $cm^{-3}$, an average value for senescent diatoms[47] which we found to be most similar to the material we observed in the ice, and a dynamic viscosity of 0.019 g $cm^{-1}$

$s^{-1}$[193], we set the average sinking rate to 1 m per day. From the width of the patch, the length and the depth we calculate the volume of the patch as a function of time.

### Sea-ice deformation measured from Synthetic Aperture Radar (SAR) satellite images

Sea-ice deformation quantifies how much a sea-ice covered area expanded, compressed or sheared which creates open water (leads) and ridges. Convergence, i.e., area compression, serves as a useful proxy for the amount of sea-ice area that underwent ridging. Thanks to the increasing availability of Synthetic Aperture Radar (SAR) satellite images in the Arctic, we can derive sea-ice deformation at daily, kilometer-scale resolution. In this study, we used sequential ESA's Sentinel-1A/B scenes along the drift track of the MOSAiC Central Observatory to calculate regularly gridded, daily sea-ice drift and deformation fields with a spatial resolution of 1.4 km following the methods described in von Albedyll et al.[51] and Krumpen et al.[57].

### Ridge areal fraction measured from Airborne Laser Scanner surveys and estimated from ICESat-2 elevation

In this study, we used 27 Airborne Laser Scanner (ALS) surveys conducted from 2 October 2019 to 22 July 2020 during MOSAiC covering 41 ± 24 $km^2$. Helicopter-based ALS Riegl VQ-580 provides values of snow surface or snow-free ice surface freeboard with kilometer-scale areal coverage, at a spatial resolution of 0.5 m, and an elevation uncertainty of 0.05 m. Freeboard conversion from ALS elevation measurements was performed using an automated open water detection scheme using differences in open water reflectance described in Hutter et al.[94]. We identified ridge sails using a 0.5 m threshold above the modal snow freeboard following Ricker et al.[95]. To estimate ridge keel areal fraction from the sail areal fraction measured by ALS, we co-located ridge surface from ALS and bottom topography from a multibeam sonar mounted on a ROV[64]. A multibeam sonar (DT101, Imagenex, Canada) mounted on a ROV (M500, Ocean Modules, Sweden) provided measurements of ice draft over an area of 350 m in diameter with 0.05 m vertical accuracy and 0.5 m horizontal resolution. A multibeam survey at a depth of 20 m was performed under Fort Ridge on 7 January 2020. Ridge keels were identified using a 0.5 m threshold below the modal ice draft. After 21 March, we used co-located surface and bottom topography of another ridge described in Salganik et al.[96], as Fort Ridge disintegrated. For each survey, we estimated the keel and sail area for the selected ridge, and we used the sail-to-keel ratio to estimate the keel areal fraction. The estimated keel-to-sail ratio gradually decreased from 4 in October to 2 in May and increased up to 6 during summer melt due to preferential snow accumulation around ridge sails in winter[97], that makes the sails look larger (wider) since the ALS will detect the snow surface (and thus the apparent sail to keel ratio will decrease).

To upscale estimates of ridge areal fraction, we used 25 × 25 $km^2$ gridded pan-Arctic ridge sail spacing and sail height estimates derived from ICESat-2 ATL07 sea ice height data using a 0.2 m threshold from Mchedlishvili et al.[56]. The ridge areal fraction was estimated as a fraction of keel width and ridge spacing. The keel width was assumed to be 36 m following the review of Arctic sea-ice ridge morphology by Strub-Klein and Sudom[49].

### Reporting summary

Further information on research design is available in the Nature Portfolio Reporting Summary linked to this article.

## Data availability

The MATLAB code for Fig. 2ab is available at: https://github.com/esalganik/Pelagic_food_webs. Environmental DNA sequencing raw data are available at the European Nucleotide Archive (ENA), from ridge samples under accession number PRJEB90852 and for non-ridge samples under PRJNA895866. Other source data used in this study are available at FigShare: https://doi.org/10.6084/m9.figshare.31865323. The source data are from the full MOSAiC datasets available at PANGAEA as follows: Cruise track: Haas, C. Links to master tracks in different resolutions of POLARSTERN cruise PS122/2, Arctic Ocean - Arctic Ocean, 2019-12-13 — 2020-02-24 (Version 2). 21022 data points PANGAEA https://doi.org/10.1594/PANGAEA.924674 (2020). Under ice water current: Baumann, T. et al. Under-ice current measurements during MOSAiC from a 75 kHz acoustic Doppler profiler. 36.7 MBytes PANGAEA https://doi.org/10.1594/PANGAEA.934792 (2021). Sea ice physical and chemical properties: Katlein, C. et al. Sea-ice draft during the MOSAiC expedition 2019/20. 114 data points PANGAEA https://doi.org/10.1594/PANGAEA.945846 (2022), Oggier, M. et al. First-year sea-ice salinity, temperature, density, oxygen and hydrogen isotope composition from the main coring site (MCS-FYI) during MOSAiC legs 1 to 4 in 2019/2020. 7847 data points PANGAEA https://doi.org/10.1594/PANGAEA.956732 (2023), Oggier, M. et al. Second-year sea-ice salinity, temperature, density, oxygen and hydrogen isotope composition from the main coring site (MCS-SYI) during MOSAiC legs 1 to 4 in 2019/2020. 9395 data points PANGAEA https://doi.org/10.1594/PANGAEA.959830 (2023), Granskog, M. A. et al. Temperature and heating induced temperature difference measurements from the sea ice mass balance buoy SIMBA 2020T60. 4 datasets Preprint at https://doi.org/10.1594/PANGAEA.924269 (2020), Salganik, E. et al. Temperature and heating-induced temperature difference measurements from Digital Thermistor Chains (DTCs) during MOSAiC 2019/2020. 24 datasets Preprint at https://doi.org/10.1594/PANGAEA.964023 (2023), Salganik, E. et al. Sea ice cores photos from Fort Ridge during MOSAiC 2019/20. 252 data points PANGAEA https://doi.org/10.1594/PANGAEA.962537 (2023), Salganik, E. et al. Drill-hole ridge ice and snow thickness and draft measurements of 'Fort Ridge' during MOSAiC 2019/20. 2258 data points PANGAEA https://doi.org/10.1594/PANGAEA.960347. Quantification of microorganisms by flow cytometry: Müller, O. et al. Flow cytometry dataset from CTD casts showing the abundance of microorganisms (smaller than 20 µm) during the Arctic MOSAiC expedition. 13768 data points PANGAEA https://doi.org/10.1594/PANGAEA.963430 (2023), Müller, O. et al. Flow cytometry dataset from first year sea ice (FYI) core bottom 5 cm sections showing the abundance of microorganisms (< 20 µm) during leg 2, 3 (February, March and April 2020) of the Arctic MOSAiC expedition. 226 data points PANGAEA https://doi.org/10.1594/PANGAEA.963560 (2023).Quantification of protists by microscopy: Assmy, P. et al. Sea-ice protist (including ice algae) abundance and biodiversity data from ice coring at the main coring sites (MCS_FYI and MCS_SYI) and ridges during MOSAiC legs 2 to 4 in 2019/2020. 51603 data points PANGAEA https://doi.org/10.1594/PANGAEA.957637 (2023), Assmy, P. et al. Pelagic protist (including phytoplankton) abundance and biodiversity data collected from the water column and water filled voids inside ridges during MOSAiC legs 2 to 4 in 2019/2020. 20913 data points PANGAEA https://doi.org/10.1594/PANGAEA.957640 (2023). Quantification of chlorophyll a: Hoppe et al. (2023): Water column Chlorophyll a concentrations during the MOSAiC expedition (PS122) in the Central Arctic Ocean 2019-2020 [dataset]. PANGAEA, https://doi.org/10.1594/PANGAEA.963277.

Received: 10 January 2025; Accepted: 27 March 2026;
Published online: 10 April 2026

## References

1. Gosselin, M., Levasseur, M., Wheeler, P. A., Horner, R. A. & Booth, B. C. New measurements of phytoplankton and ice algal production in the Arctic Ocean. *Deep Sea Res. Part II Top. Stud. Oceanogr.* **44**, 1623–1644 (1997).
2. Azam, F. et al. The Ecological Role of Water-Column Microbes in the Sea. *Mar. Ecol. Prog. Ser.* **10**, 257–263 (1983).
3. Kirchman, D. L., Morán, X. A. G. & Ducklow, H. Microbial growth in the polar oceans — role of temperature and potential impact of climate change. *Nat. Rev. Microbiol.* **7**, 451–459 (2009).
4. Rudels, B. & Carmack, E. Arctic Ocean Water Mass Structure and Circulation. *Oceanography*, https://doi.org/10.5670/oceanog.2022.116 (2022).

5. Rehder, L. et al. Different temperature sensitivities of key physiological processes lead to divergent trait response patterns in Arctic phytoplankton. *Limnol. Oceanogr.* **69**, 1845–1856 (2024).
6. Coello-Camba, A. & Agustí, S. Thermal Thresholds of Phytoplankton Growth in Polar Waters and Their Consequences for a Warming Polar Ocean. *Front. Mar. Sci.* **4**, 168 (2017).
7. Børsheim, K. Y. & Drinkwater, K. F. Different temperature adaptation in Arctic and Atlantic heterotrophic bacteria in the Barents Sea Polar Front region. *J. Mar. Syst.* **130**, 160–166 (2014).
8. Berge, J. et al. In the dark: A review of ecosystem processes during the Arctic polar night. *Prog. Oceanogr.* **139**, 258–271 (2015).
9. Berge, J., Johnsen, G. & Cohen, J. H. Introduction. in POLAR NIGHT Marine Ecology (eds. Berge, J., Johnsen, G. & Cohen, J. H.) vol. 4 1–15 (Springer International Publishing, Cham, 2020).
10. Sherr, E. B., Sherr, B. F., Wheeler, P. A. & Thompson, K. Temporal and spatial variation in stocks of autotrophic and heterotrophic microbes in the upper water column of the central Arctic Ocean. *Deep Sea Res. Part Oceanogr. Res. Pap.* **50**, 557–571 (2003).
11. Vaqué, D. et al. Seasonal changes in planktonic bacterivory rates under the ice-covered coastal Arctic Ocean. *Limnol. Oceanogr.* **53**, 2427–2438 (2008).
12. Garneau, M., Roy, S., Lovejoy, C., Gratton, Y. & Vincent, W. F. Seasonal dynamics of bacterial biomass and production in a coastal arctic ecosystem: Franklin Bay, western Canadian Arctic. *J. Geophys. Res. Oceans* **113**, 2007JC004281 (2008).
13. Anderson, S. R. & Menden-Deuer, S. Growth, Grazing, and Starvation Survival in Three Heterotrophic Dinoflagellate Species. *J. Eukaryot. Microbiol.* **64**, 213–225 (2017).
14. Gradinger, R. Vertical fine structure of the biomass and composition of algal communities in Arctic pack ice. *Mar. Biol.* **133**, 745–754 (1999).
15. Olsen, L. M. et al. The seeding of ice algal blooms in Arctic pack ice: The multiyear ice seed repository hypothesis: Seeding of Ice Algae in Arctic Pack Ice. *J. Geophys. Res. Biogeosciences* **122**, 1529–1548 (2017).
16. Untersteiner, N. Natural desalination and equilibrium salinity profile of perennial sea ice. *J. Geophys. Res.* **73**, 1251–1257 (1968).
17. Golden, K. M., Ackley, S. F. & Lytle, V. I. The Percolation Phase Transition in Sea Ice. *Science* **282**, 2238–2241 (1998).
18. Hopkins, M. A. & Thorndike, A. S. Floe formation in Arctic sea ice. *J. Geophys. Res. Oceans* **111**, 2005JC003352 (2006).
19. Hopkins, M. A. Four stages of pressure ridging. *J. Geophys. Res. Oceans* **103**, 21883–21891 (1998).
20. Rothrock, D. A. & Zhang, J. Arctic Ocean sea ice volume: What explains its recent depletion? *J. Geophys. Res. Oceans* **110**, 2004JC002282 (2005).
21. Mårtensson, S., Meier, H. E. M., Pemberton, P. & Haapala, J. Ridged sea ice characteristics in the Arctic from a coupled multicategory sea ice model. *J. Geophys. Res. Oceans* **117**, 2010JC006936 (2012).
22. Hansen, E. et al. Variability in categories of Arctic sea ice in Fram Strait. *J. Geophys. Res. Oceans* **119**, 7175–7189 (2014).
23. Frederking, R. & Wright, B. Characteristics and stability of an ice rubble field, Issungnak, February-March 1980. *Can. Natl. Res. Counc. Associate Comm. Geotech. Res. Tech. Memorandum* **134**, 230–247 (1980).
24. Nicolaus, M. et al. Overview of the MOSAiC expedition: Snow and sea ice. *Elem. Sci. Anth* **10**, 000046 (2022).
25. Fong, A. A. et al. Overview of the MOSAiC expedition: Ecosystem. *Elem. Sci. Anth* **12**, 00135 (2024).
26. Granskog, M. & Müller, O. A peek beneath the surface of Arctic sea ice. *EU Res* **37**, 38–39 (2024).
27. Dolan, J. R., Pierce, R. W. & Yang, E. J. Tintinnid ciliates of the marine microzooplankton in Arctic Seas: a compilation and analysis of species records. *Polar Biol.* **40**, 1247–1260 (2017).
28. Hoppe, C. J. M. et al. Photosynthetic light requirement near the theoretical minimum detected in Arctic microalgae. *Nat. Commun.* **15**, 7385 (2024).
29. Dolan, J. R. et al. Microzooplankton in a Warming Arctic: A Comparison of Tintinnids and Radiolarians from Summer 2011 and 2012 in the Chukchi Sea. *Acta Protozoologica* **53**, 101–113 (2014).
30. Li, H. et al. Boreal Tintinnid Assemblage in the Northwest Pacific and Its Connection with the Japan Sea in Summer 2014. *PLOS ONE* **11**, e0153379 (2016).
31. Monti, M. & Minocci, M. Microzooplankton along a transect from northern continental Norway to Svalbard. *Polar Res* **32**, 19306 (2013).
32. Wilson, B. et al. Changes in Marine Prokaryote Composition with Season and Depth Over an Arctic Polar Year. *Front. Mar. Sci.* **4**, 95 (2017).
33. Ameryk, A., Jankowska, K. M., Kalinowska, A. & Węsławski, J. M. Comparison of bacterial production in the water column between two Arctic fjords, Hornsund and Kongsfjorden (West Spitsbergen). *Oceanologia* **59**, 496–507 (2017).
34. Jakobsen, H. & Hansen, P. Prey size selection, grazing and growth response of the small heterotrophic dinoflagellate Gymnodinium sp. and the ciliate Balanion comatum-a comparative study. *Mar. Ecol. Prog. Ser.* **158**, 75–86 (1997).
35. Fenchel, T. Ecology of Heterotrophic Microflagellates. II. Bioenergetics and Growth. *Mar. Ecol. Prog. Ser.* **8**, 225–231 (1982).
36. Straile, D. Gross growth efficiencies of protozoan and metazoan zooplankton and their dependence on food concentration, predator-prey weight ratio, and taxonomic group. *Limnol. Oceanogr.* **42**, 1375–1385 (1997).
37. Rose, J. M., Vora, N. M., Countway, P. D., Gast, R. J. & Caron, D. A. Effects of temperature on growth rate and gross growth efficiency of an Antarctic bacterivorous protist. *ISME J.* **3**, 252–260 (2009).
38. Olsen, L. M., Reinertsen, H. & Vadstein, O. Can Phosphorus Limitation Inhibit Dissolved Organic Carbon Consumption in Aquatic Microbial Food Webs? A Study of Three Food Web Structures in Microcosms. *Microb. Ecol.* **43**, 353–366 (2002).
39. Montagnes, D. Ecophysiology and behavior of tintinnids. in The Biology and Ecology of Tintinnid Ciliates: Models for Marine Plankton 85–121 (Wiley-Blackwell, Oxford, 2012).
40. McManus, G. B. & Fuhrman, J. Clearance of Bacteria-Sized Particles by Natural Populations of Nanoplankton in the Chesapeake Bay Outflow Plume. *Mar. Ecol. Prog. Ser.* **42**, 199–206 (1988).
41. Strom, S. Growth and grazing rates of the herbivorous dinoflagellate Gymnodinium sp. from the open subarctic Pacific Ocean. *Mar. Ecol. Prog. Ser.* **78**, 103–113 (1991).
42. Cox, G. F. N. & Weeks, W. F. Equations for Determining the Gas and Brine Volumes in Sea-Ice Samples. *J. Glaciol.* **29**, 306–316 (1983).
43. Garrison, D. L. & Buck, K. R. Organism losses during ice melting: A serious bias in sea ice community studies. *Polar Biol.* **6**, 237–239 (1986).
44. Chamberlain, E. J. et al. Impacts of sea ice melting procedures on measurements of microbial community structure. *Elem. Sci. Anthr.* **10**, 00017 (2022).
45. Dolan, J. R., Landry, M. R. & Ritchie, M. E. The species-rich assemblages of tintinnids (marine planktonic protists) are structured by mouth size. *ISME J.* **7**, 1237–1243 (2013).
46. García-Oliva, O. & Wirtz, K. Size-dependent and -independent prey selection of dinoflagellates. *Mar. Biol.* **169**, 122 (2022).
47. Eppley, R. W., Holmes, R. W. & Strickland, J. D. H. Sinking rates of marine phytoplankton measured with a fluorometer. *J. Exp. Mar. Biol. Ecol.* **1**, 191–208 (1967).
48. Salganik, E. et al. Drill-hole ridge ice and snow thickness and draft measurements of 'Fort Ridge' during MOSAiC 2019/20. 2258 data points PANGAEA https://doi.org/10.1594/PANGAEA.960347 (2023).

49. Strub-Klein, L. & Sudom, D. A comprehensive analysis of the morphology of first-year sea ice ridges. *Cold Reg. Sci. Technol.* **82**, 94–109 (2012).
50. Guzenko, R. B. et al. Morphometry and Internal Structure of Ice Ridges and Stamukhas in the Kara, Laptev and East Siberian Seas. Results of 2013-2017 Field Studies. *SSRN Electron. J.* https://doi.org/10.2139/ssrn.4359510 (2023)
51. von Albedyll, L. Sea ice deformation and sea ice thickness change. (Universität Bremen, 2022). https://doi.org/10.26092/ELIB/1868.
52. Hutter, N. et al. Sea Ice Rheology Experiment (SIREx): 2. Evaluating linear kinematic features in high-resolution sea ice simulations. *J. Geophys. Res. Oceans: Oceans* **127**, e2021JC017666 (2022).
53. Salganik, E., Høyland, K. V. & Maus, S. Consolidation of fresh ice ridges for different scales. *Cold Reg. Sci. Technol.* **171**, 102959 (2020).
54. Chen, X., Høyland, K. V. & Ji, S. Laboratory tests to investigate the initial phase of ice ridge consolidation. *Cold Reg. Sci. Technol.* **176**, 103093 (2020).
55. Shestov, A. & Marchenko, A. Properties of Ice Ridge Keels and Sea Currents in their Vicinity in the Barents Sea. https://doi.org/10.13140/2.1.2955.2004 (2014)
56. Mchedlishvili, A., Lüpkes, C., Petty, A., Tsamados, M. & Spreen, G. New estimates of pan-Arctic sea ice–atmosphere neutral drag coefficients from ICESat-2 elevation data. *Cryosphere* **17**, 4103–4131 (2023).
57. Krumpen, T. et al. MOSAiC drift expedition from October 2019 to July 2020: sea ice conditions from space and comparison with previous years. *Cryosphere* **15**, 3897–3920 (2021).
58. Hibler, W. D., Weeks, W. F. & Mock, S. J. Statistical aspects of sea-ice ridge distributions. *J. Geophys. Res.* **77**, 5954–5970 (1972).
59. Williams, E., Charles, S. & Robin, G. D. Q. A Submarine Sonar Study of Arctic Pack Ice. *J. Glaciol.* **15**, 349–362 (1975).
60. Jahn, A., Holland, M. M. & Kay, J. E. Projections of an ice-free Arctic Ocean. *Nat. Rev. Earth Environ.* **5**, 164–176 (2024).
61. Krumpen, T. et al. Arctic warming interrupts the Transpolar Drift and affects long-range transport of sea ice and ice-rafted matter. *Sci. Rep.* **9**, 5459 (2019).
62. Krumpen, T. et al. The MOSAiC ice floe: sediment-laden survivor from the Siberian shelf. *Cryosphere* **14**, 2173–2187 (2020).
63. Haas, C. & Rabe, B. The Expedition PS122/2 of the Research Vessel POLARSTERN to the Arctic Ocean in 2019/2020. (2023).
64. Katlein, C. et al. A New Remotely Operated Sensor Platform for Interdisciplinary Observations under Sea Ice. *Front. Mar. Sci.* **4**, 281 (2017).
65. Anhaus, P. et al. Under-ice environment observations from a remotely operated vehicle during the MOSAiC expedition. *Sci. Data* **12**, 944 (2025).
66. Wollenburg, J. E. et al. New observations of the distribution, morphology and dissolution dynamics of cryogenic gypsum in the Arctic Ocean. *Cryosphere* **14**, 1795–1808 (2020).
67. Campbell, K. et al. Melt Procedure Affects the Photosynthetic Response of Sea Ice Algae. *Front. Earth Sci.* **7**, 21 (2019).
68. Oggier, M. et al. First-year sea-ice salinity, temperature, density, oxygen and hydrogen isotope composition from the main coring site (MCS-FYI) during MOSAiC legs 1 to 4 in 2019/2020. 7847 data points PANGAEA https://doi.org/10.1594/PANGAEA.956732 (2023).
69. Oggier, M. et al. Second-year sea-ice salinity, temperature, density, oxygen and hydrogen isotope composition from the main coring site (MCS-SYI) during MOSAiC legs 1 to 4 in 2019/2020. 9395 data points PANGAEA https://doi.org/10.1594/PANGAEA.959830 (2023).
70. Granskog, M. A. et al. Temperature and heating induced temperature difference measurements from the sea ice mass balance buoy SIMBA 2020T60. [dataset bundled publication]. PANGAEA, https://doi.org/10.1594/PANGAEA.924269 (2020).
71. Salganik, E. et al. Temperature and heating induced temperature difference measurements from Digital Thermistor Chains (DTCs) during MOSAiC 2019/2020 [dataset bibliography]. PANGAEA, https://doi.org/10.1594/PANGAEA.964023 (2023).
72. Rabe, B. et al. Overview of the MOSAiC expedition: Physical oceanography. *Elem. Sci. Anth* **10**, 00062 (2022).
73. Marie, D., Brussaard, C. P. D., Thyrhaug, R., Bratbak, G. & Vaulot, D. Enumeration of Marine Viruses in Culture and Natural Samples by Flow Cytometry. *Appl. Environ. Microbiol.* **65**, 45–52 (1999).
74. Lee, S. & Fuhrman, J. A. Relationships between Biovolume and Biomass of Naturally Derived Marine Bacterioplankton. *Appl. Environ. Microbiol.* **53**, 1298–1303 (1987).
75. Zubkov, M. V., Burkill, P. H. & Topping, J. N. Flow cytometric enumeration of DNA-stained oceanic planktonic protists. *J. Plankton Res.* **29**, 79–86 (2007).
76. Borsheim, K. & Bratbak, G. Cell volume to cell carbon conversion factors for a bacterivorous Monas sp. enriched from seawater. *Mar. Ecol. Prog. Ser.* **36**, 171–175 (1987).
77. Edler, L., Elbrächter, M. The Utermöhl method for quantitative phytoplankton analysis. in Microscopic and Molecular Methods for Quantitative Phytoplankton Analysis 13–20 (United Nations Educational, Scientific and Cultural Organization (UNESCO), Paris, 2010).
78. Hillebrand, H., Dürselen, C., Kirschtel, D., Pollingher, U. & Zohary, T. BIOVOLUME CALCULATION FOR PELAGIC AND BENTHIC MICROALGAE. *J. Phycol.* **35**, 403–424 (1999).
79. Menden-Deuer, S. & Lessard, E. J. Carbon to volume relationships for dinoflagellates, diatoms, and other protist plankton. *Limnol. Oceanogr.* **45**, 569–579 (2000).
80. Holm-Hansen, O. & Riemann, B. Chlorophyll a Determination: Improvements in Methodology. *Oikos* **30**, 438 (1978).
81. Ovreås, L., Forney, L., Daae, F. L. & Torsvik, V. Distribution of bacterioplankton in meromictic Lake Saelenvannet, as determined by denaturing gradient gel electrophoresis of PCR-amplified gene fragments coding for 16S rRNA. *Appl. Environ. Microbiol.* **63**, 3367–3373 (1997).
82. Apprill, A., McNally, S., Parsons, R. & Weber, L. Minor revision to V4 region SSU rRNA 806R gene primer greatly increases detection of SAR11 bacterioplankton. *Aquat. Microb. Ecol.* **75**, 129–137 (2015).
83. Medlin, L., Elwood, H. J., Stickel, S. & Sogin, M. L. The characterization of enzymatically amplified eukaryotic 16S-like rRNA-coding regions. *Gene* **71**, 491–499 (1988).
84. P H Weekers, R J Gast, P A Fuerst, T J Byers. Sequence variations in small-subunit ribosomal RNAs of Hartmannella vermiformis and their phylogenetic implications. *Mol. Biol. Evol.* https://doi.org/10.1093/oxfordjournals.molbev.a040147 (1994).
85. Callahan, B. J. et al. DADA2: High-resolution sample inference from Illumina amplicon data. *Nat. Methods* **13**, 581–583 (2016).
86. R Core Team. R: A language and environment for statistical computing. R Foundation for Statistical Computing, Vienna, Austria (2021).
87. Quast, C. et al. The SILVA ribosomal RNA gene database project: improved data processing and web-based tools. *Nucleic Acids Res* **41**, D590–D596 (2012).
88. Guillou, L. et al. The Protist Ribosomal Reference database (PR2): a catalog of unicellular eukaryote Small Sub-Unit rRNA sequences with curated taxonomy. *Nucleic Acids Res* **41**, D597–D604 (2012).
89. Smith, D. C. & Azam, F. A simple, economical method for measuring bacterial protein synthesis rates in seawater using 3H-leucine. *Mar. Microb. Foodwebs* **6**, 107–114 (1992).
90. Dagestad, Röhrs, K.-F., Breivik, J. & Ådlandsvik, Ø B. OpenDrift v1.0: a generic framework for trajectory modelling. *Geosci. Model Dev.* **11**, 1405–1420 (2018).
91. Baumann, T. et al. Under-ice current measurements during MOSAiC from a 75 kHz acoustic Doppler profiler. 36MBytes PANGAEA https://doi.org/10.1594/PANGAEA.934792 (2021).
92. Sakov, P. et al. TOPAZ4: an ocean-sea ice data assimilation system for the North Atlantic and Arctic. *Ocean Sci.* **8**, 633–656 (2012).

93. Sharqawy, M. H., Lienhard, J. H. & Zubair, S. M. Thermophysical properties of seawater: a review of existing correlations and data. *Desalination Water Treat.* **16**, 354–380 (2010).
94. Hutter, N. et al. Digital elevation models of the sea-ice surface from airborne laser scanning during MOSAiC. *Sci. Data* **10**, 729 (2023).
95. Ricker, R. et al. Linking scales of sea ice surface topography: evaluation of ICESat-2 measurements with coincident helicopter laser scanning during MOSAiC. *Cryosphere* **17**, 1411–1429 (2023).
96. Salganik, E. et al. Different mechanisms of Arctic first-year sea-ice ridge consolidation observed during the MOSAiC expedition. *Elem. Sci. Anth* **11**, 00008 (2023).
97. Itkin, P. et al. Sea ice and snow characteristics from year-long transects at the MOSAiC Central Observatory. *Elem. Sci. Anthr.* **11**, 00048 (2023).
98. Jakobsson, M. et al. The International Bathymetric Chart of the Arctic Ocean Version 4.0. *Sci. Data* **7**, 176 (2020).
99. Katlein, C. et al. Sea-ice draft during the MOSAiC expedition 2019/20. 114 data points PANGAEA https://doi.org/10.1594/PANGAEA.945846 (2022).

## Acknowledgements

This work was funded by the Research Council of Norway through project HAVOC (grant no 280292). ES was supported by the Research Council of Norway project INTERAAC (grant no. 328957). BAL and MAG were supported by the Research Council of Norway project CAATEX (grant no. 280531). PA was funded by the Centre for ice, Cryosphere, Carbon and Climate (iC3) supported by the Research Council of Norway through its Centres of Excellence funding scheme, project number 332635. MAG also acknowledges the fellowship support from Hanse-Wissenschaftskolleg Institute of Advanced Study (Delmenhorst, Germany). This work was carried out and data used in this manuscript was produced as part of the international Multidisciplinary drifting Observatory for the Study of the Arctic Climate (MOSAiC) with the tag MOSAiC20192020. We thank all persons involved in the expedition of the Research Vessel Polarstern during MOSAiC in 2019-2020 (AWI_PS122_00) as listed in Nixdorf et al. (2021). Thanks to the captain and crew of Polarstern, team ECO and team ICE, and the entire MOSAiC science team on leg 2, Egor Shimanchuk and Giulia Castellani for help with field work, Miriam Marquardt for chlorophyll analysis, and Irene Heggdal at ELMILAB for help with SEM. We thank Laura Heitmann, Tina Brenneis, and Anja Terbrüggen for help with Chl a measurements, and Benoit Lebreton and Gaël Guillou for POC analyses. Tatiana Tsagkaraki for flow cytometry gating plots, Marit Reigstad for constructive comments, and Frida Cnossen for drawing the background of Fig. 2c.

## Author contributions

Lasse Mork Olsen: Conceptualization, Methodology, Formal analysis, Investigation, Data curation, Writing – Original draft preparation, Visualization, Writing – Review & Editing. Evgenii Salganik: Data curation, Formal analysis, Writing – Original draft preparation, Visualization, Writing – Review & Editing. Oliver Müller: Methodology, Formal analysis, Investigation, Data curation, Visualization, Writing – Review & Editing. Luisa von Albedyll: Methodology, Writing – Review & Editing. Philipp Assmy: Conceptualization, Methodology, Resources, Supervision, Project administration, Funding acquisition, Writing – Review & Editing. Mats A. Granskog: Conceptualization, Supervision, Resources, Project administration, Funding acquisition, Writing - Review & Editing. Clara J.M. Hoppe: Methodology, Investigation, Data curation, Resources, Funding acquisition, Writing – Review & Editing. Robert G. Campbell: Investigation, Resources, Writing – Review & Editing. Aud Larsen: Conceptualization, Methodology, Resources, Supervision, Project administration, Funding acquisition, Writing – Review & Editing. Eva Leu: Conceptualization, Methodology, Funding acquisition, Writing – Review & Editing. Rolf Gradinger: Conceptualization, Methodology, Resources, Supervision, Project administration, Funding acquisition, Writing – Review & Editing. Jessie Gardner: Investigation, Data curation, Writing – Review & Editing. Nicole Aberle: Funding acquisition, Writing – Review & Editing. Dmitry V. Divine: Methodology, Investigation, Resources, Writing – Review & Editing. Knut V. Høyland: Conceptualization, Resources, Funding acquisition, Writing - Review & Editing. Christian Katlein: Methodology, Investigation, Resources, Writing – Review & Editing. Benjamin A. Lange: Methodology, Writing – Review & Editing. Agnieszka Tatarek: Methodology, Investigation, Data curation, Writing – Review & Editing. Jozef Wiktor: Methodology, Investigation, Data curation, Writing – Review & Editing. Gunnar Bratbak: Conceptualization, Methodology, Resources, Data curation, Supervision, Project administration, Funding acquisition, Writing – Review & Editing.

## Funding

Open access funding provided by University of Bergen.

## Competing interests

The authors declare no competing interests.

## Additional information

**Supplementary information** The online version contains supplementary material available at https://doi.org/10.1038/s43247-026-03486-z.

**Correspondence** and requests for materials should be addressed to Lasse Mork Olsen.

**Peer review information** *Communications Earth & Environment* thanks Jodi Young and the other, anonymous, reviewer(s) for their contribution to the peer review of this work. Primary Handling Editors: Michael Stukel, Alice Drinkwater, and Mengjie Wang. A peer review file is available.